Available online at www.sciencedirect.com
ScienceDirect
Trans. Nonferrous Met. Soc. China 25(2015) 4080−4088
Transactions of Nonferrous Metals Society of China
www.tnmsc.cn

Atomistic simulation of defected magnesium hydroxide as flame retardants

Dong-yun ZHANG[1,2,3], Ping YANG[1], Zheng DU[2], Qiu-hua YUAN[1],
Shen-hua SONG[3], Xiang-zhong REN[1], Pei-xin ZHANG[1]

1. College of Chemistry and Environmental Engineering, Shenzhen University, Shenzhen 518060, China;
2. National Supercomputing Center in Shenzhen, Shenzhen 518055, China;
3. School of Materials Science and Engineering, Harbin Institute of Technology Shenzhen Graduate School, Shenzhen 518055, China

Received 18 May 2015; accepted 12 October 2015

Abstract: The mechanical properties and the point defect energy of magnesium hydroxide ($Mg(OH)_2$) were studied using the molecular dynamics. Moreover, the microelectronic structure of $Mg(OH)_2$ with point defects in the bulk and on its surface were investigated using the first principles. The simulation results indicate that $Mg(OH)_2$ was easily modified by other cations because of its strong, favorable interstitial and substitution defects via point defect energy calculation. $Mg(OH)_2$ can provide high-efficiency flame retardancy because of the strong OH (OH Schottky defect) or H bond (H Frenkel defect and Schottky defect). The potential model of $Mg(OH)_2$ was established, and molecular dynamics simulation was used to investigate the relations between the crystal structure and the mechanical properties. $Mg(OH)_2$ with special morphology such as nano-sheets was a prior consideration to maintain the composite mechanical properties. The detailed electronic structures of $Mg(OH)_2$ with defects were determined. This work may provide theoretical guidance for choosing dopant element and reveal the element doping mechanism of $Mg(OH)_2$.
Key words: $Mg(OH)_2$; density functional theory; molecular dynamics; defects; electronic structure

1 Introduction

Magnesium hydroxide ($Mg(OH)_2$) is an important inorganic material that has many important industrial applications [1]. It is widely used in polymer materials as an environment-friendly additive-type flame retardant [2,3]. Flame retardants are additives that inhibit or resist the spread of fire when they are used in polymer products, such as plastics, rubber, fibers, woods, and textiles. Flame retardant technology is gaining increased attention because of the social requirements for safety in the use of polymer materials. $Mg(OH)_2$ is a non-halogenated flame retardant that shows excellent properties, such as suitability for plastics at higher processing temperatures, smoke suppression, no evolution of hazardous by-products, and fire-retarding properties [4]. There are a lot of researches showing that the morphology and size of $Mg(OH)_2$ can significantly influence the mechanical properties of doped polymer materials [5,6], and $Mg(OH)_2$ can be better applied in various flame retardants by purification, micronization, and surface modification [7−9].

Different particle sizes and shapes of $Mg(OH)_2$ can be synthesized by solvent molecules [10] or introducing cations with diverse valents [11], which results in defect formation. PANG et al [11,12] produced lamellar (nano-sheets), rose-like, and torispherical $Mg(OH)_2$ by introducing cations of varying valents (Zn^{2+}, Al^{3+}, and Sn^{4+}), and they proposed valence bonding to the cations as the differentiating mechanism. Defect problems are critical to modern solid science and technology. The formation of an interface defect is easy because of the large specific surface area and high surface energy of nano-$Mg(OH)_2$, which results in the decline of some polymer functions. Therefore, point defect is an important factor affecting many flame retardant properties, from phase stability to morphology to usage [13]. The existence of defects in condensed matter can be experimentally detected and measured by positron annihilation techniques, extended X-ray absorption fine-structure, X-ray absorption near-edge spectroscopy,

Foundation item: Projects (51174138, 20971088) supported by the National Natural Science Foundation of China; Project (JCYJ20130329102720840) supported by Shenzhen Government's Plan of Science and Technology, China
Corresponding author: Pei-xin ZHANG; Tel: +86-755-26733136; E-mail: pxzhang@szu.edu.cn
DOI: 10.1016/S1003-6326(15)64058-4

and neutron diffraction [14−17]. However, these techniques are not widely used because of their complexity process and comparatively high cost. Meanwhile, computations can contribute to the understanding of point defects [18−20]. To the best of our knowledge, the defects of $Mg(OH)_2$ have not yet been investigated from this perspective.

In the present work, the detailed microstructures of $Mg(OH)_2$ containing point defects both in the bulk and on its surface were determined using density functional theory. The crystal and electronic structures of $Mg(OH)_2$ with ions dopants were studied to provide theoretical direction to selecting the modified ions. Furthermore, molecular dynamics (MD) simulation was used to investigate the mechanical properties and the effects on defect energies of different defects [21,22]. The purpose was to provide technical guidance for modifying and using composite $Mg(OH)_2$, and provide methods and scientific basis for looking for other high-efficiency flame retardants. Moreover, a detailed study on the elastic constants of $Mg(OH)_2$ can provide important information for the mechanical performances of $Mg(OH)_2$ combined with polymer materials too.

2 Computational methods and theory

$Mg(OH)_2$ (trigonal, space group $P\bar{3}m1$, No. 164, Z=1) has a layered CdI_2-type structure. The layer structure has one layer of Mg and two layers of hydroxyl (OH) groups. The OH groups are bonded to three Mg cations (Fig. 1) [23].

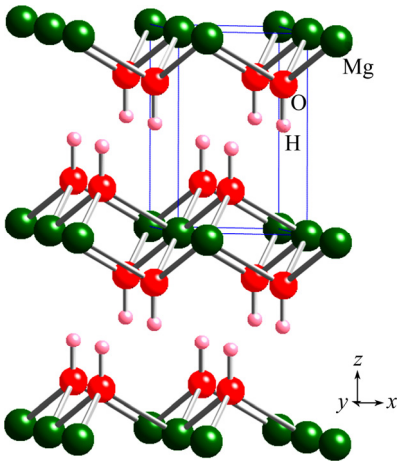

Fig. 1 Structure of magnesium hydroxide (Big green ball represents Mg, medium red ball represents O, and small pink ball represents H)

2.1 Model with point defects using MD

All of these calculations were performed on supercomputers in National Supercomputing Center in Shenzhen. MD was used to investigate the point defects energies and the mechanic properties of $Mg(OH)_2$. The calculation used the Mott−Littleton method implemented in the General Utility Lattice Program (GULP) [24]. This method partitions the crystal lattice surrounding the defect into two spherical regions. In the inner sphere, the ions are strongly displaced by the defect; thus, the interactions are explicitly treated and the ions are allowed to relax completely. By contrast, the ions in the outer region are implicitly treated as a dielectric continuum. The obtained radii of the inner and outer spheres were 10 and 20 Å, i.e., regions I and II contained ~750 and ~5100 ions, respectively.

The interactions between ions in the crystalline $Mg(OH)_2$ compose long-range Coulombic and short-range interaction components. The interatomic potentials of O and H from 0 Å to 1.2 Å are expressed as Morse forms as Eq. (1):

$$V(r_{ij}) = D_e[(1-\exp(-a_0(r_{ij}-r_0)))^2-1] \quad (1)$$

where r_{ij} is the distance between atoms i and j, and D_e (eV), a_0, and r_0 (Å) are the empirical parameters.

Other short-range interactions, including the interaction of O and H from 1.2 Å to 10.0 Å, are modeled using the Buckingham potential function given by Eq. (2):

$$V(r_{ij}) = A\exp\left(-\frac{r_{ij}}{\rho_{ij}}\right)-\frac{C}{r^6} \quad (2)$$

where A (eV), ρ_{ij} (Å), and C (eV·Å^6) are the empirical parameters. The interatomic potentials for Mg^{2+}, H^+, and O^{2-} are fitted based on the study of GALE [25] on oxide materials (Table 1).

Table 1 Parameters of general interatomic potentials for $Mg(OH)_2$

Interaction	Potential	D_e/eV	a_0	r_0/Å	Cutoffs range/Å	
					Min	Max
H—O	Morse	5.539	2.3669	0.966	0	1.2

Interaction	Potential	A/eV	ρ_{ij}/Å	C/(eV·Å^6)	Cutoffs range/Å	
					Min	Max
H—O	Buckingham	616.71	0.25	0	1.2	10
O—O	Buckingham	22764.3	0.149	30.72	0	18
Mg—O	Buckingham	1862.9	0.2747	0	0	10
Ca—O	Buckingham	2100	0.302	0	0	10

The $Mg(OH)_2$ structure was optimized under constant pressure (0 Pa). The charges of O, H, and Mg were set to −1.59, 0.59 and 2.0, respectively, based on the atomic population analysis in the Mulliken area through first principles calculation. The unit-cell parameters and bond lengths obtained were compared with the experimental values and ab initio calculations in Table 2 and good agreement had been achieved. The

Table 2 Calculated and experimental structural parameters of $Mg(OH)_2$

Reference	Unit-cell parameters		Bond length/Å			Fractional coordinate	
	a/Å	*c*/Å	Mg—O	H—O	H⋯H	*z*(O)	*z*(H)
Experiment [26]	0.413	3.150	4.770	2.100	1.997	0.919	0.220
Experiment [25]	0.430	3.142	4.766	2.099	−	0.995	0.222
MD (this work)	3.143	4.709	2.090	0.890	−	0.220	0.402
Calculated (ab initio) [26]	3.148	5.263	2.093	0.940	−	−	−
Calculated (ab initio) (this work)	3.161	4.696	2.093	0.943	1.977	0.419	0.218

discrepancy between the experimental and calculated values of the parameters describing the interlayer distance (*c* axis) was somewhat higher than that of the parameters describing the intralayer distance (*a* axis and Mg—O distance). However, the discrepancies were within the acceptable margin.

2.2 Model with point defects using first principles

The calculations were performed using CASTEP [27], an ab initio quantum program based on density functional theory (DFT). Simulation details are shown in Table 3. The lattice parameters of the optimized $Mg(OH)_2$ are shown in Table 2 and agree well with each other [25,26]. In Ref. [26], $Mg(OH)_2$ was investigated theoretically using an ab initio all-electron linear combination of atomic orbitals Hartree−Fock (HF) approximation. The interlayer interaction is weak at the HF level and leads to larger interlayer distance compared with the experimental one.

Table 3 Simulation details of CASTEP

Simulation parameter	Value
Exchange-correlation function	GGA−PBE
Cut-off energy/eV	550
Pseudopotential	Norm-conserving
k-point	5×5×4
SCF of every atom/eV	1.0×10^{-6}
Optimization method	BFGS
Total energy convergence	0.100×10^{-4}
Max ionic force tolerance/(ev·Å^{-1})	0.030
Max ionic displacement tolerance/Å	0.100×10^{-2}
Max stress component tolerance/GPa	0.050

A model with defects was created using a 3×3×5 supercell of geometry optimized $Mg(OH)_2$ with 225 total atoms. The $Mg(OH)_2$ model with point defects was established by replacing M (M = Al, Ca, Fe, Zn) atoms in the Mg position (1/3, 1/3, 3/5) of the internal lattice of a standard $Mg(OH)_2$. Periodic boundary conditions were used so that the doped position was equivalent to all others. Surface defects were created by replacing one Mg on the surface with M atoms and cleaving through (001). For example, $Mg(OH)_2$ doped with Fe in the bulk was created as shown in Fig. 2(a), and $Mg(OH)_2$ surface (001) doped with Ca was created as shown in Fig. 2(b). The electronic structure of these models was analyzed after the geometry optimization.

3 Results

3.1 Point defects energies via MD

Both intrinsic and extrinsic defects (mainly dopant substitution) were studied by calculating the point defect energies for vacancies and interstitials and relevant lattice energies. The defects are expressed by the Kröger–Vink notation as follows:

H Frenkel:

$$H_H^X \rightarrow V_H' + H_i^{\cdot} \quad (3)$$

OH Frenkel:

$$OH_{OH}^X \rightarrow V_{OH}^{\cdot} + OH_i' \quad (4)$$

Mg Frenkel:

$$Mg_{Mg}^X \rightarrow V_{Mg}'' + Mg_i^{\cdot\cdot} \quad (5)$$

Mg Schottky:

$$Mg_{Mg}^X \rightarrow V_{Mg}^{\cdot\cdot} + e'' \quad (6)$$

H Schottky:

$$H_H^X \rightarrow V_H^{\cdot} + e' \quad (7)$$

OH Schottky:

$$OH_{OH}^X \rightarrow V_{OH}' + h^{\cdot} \quad (8)$$

Ca substitution:

$$CaO + Mg_{Mg}^X \rightarrow Ca_{Mg}^X + MgO \quad (9)$$

Ca interstitial:

$$Ca^{2+} \rightarrow Ca_i + h^{\cdot\cdot} \quad (10)$$

Table 4 lists the calculated defect formation energies. The results show that the formation of defects remarkably differs. The Schottky defect formed more difficultly than the Frenkel defect.

Table 4 Defect energies in $Mg(OH)_2$

Defect	Energy/eV
H Frenkel	17.239
OH Frenkel	4.152
Mg Frenkel	3.100×10^{-6}–4.262
H Schottky	20.364
OH Schottky	36.342
Mg Schottky	18.425
Ca substitution	3.984
Ca interstitial	−10.641

3.2 Mechanical properties via MD

The calculated elastic constants are shown in Table 5. The elastic constants represent the second derivatives of the energy density with respect to strain:

Table 5 Elastic constants of $Mg(OH)_2$

Elastic constant	Ref. [28]	This work
C_{11}	156. 7	196.6
C_{33}	46.3	40.8
C_{44}	21.7	24.4
C_{12}	44.4	59.8
C_{13}	12.0	17.4

$$C_{ij}=\frac{1}{V}\left(\frac{\partial^2 U}{\partial\varepsilon_i\partial\varepsilon_j}\right) \tag{11}$$

where U is the Helmholtz free-energy, ε_i and ε_j (i, j=1, ⋯, 6) are the components of the strain tensors ε.

Elastic constants under different pressures (0−10 GPa) were studied as shown in Figs. 3(a) and (b). C_{11} and C_{33} increase with increasing pressures, which

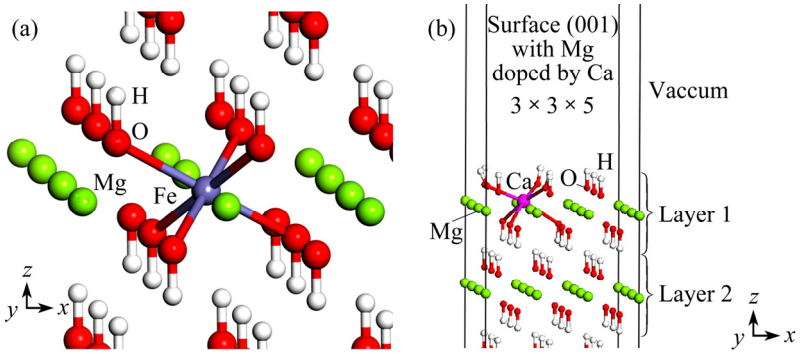

Fig. 2 Crystal structure of $Mg(OH)_2$ containing defect: (a) Doped defect in bulk; (b) Doped defect on surface (001)

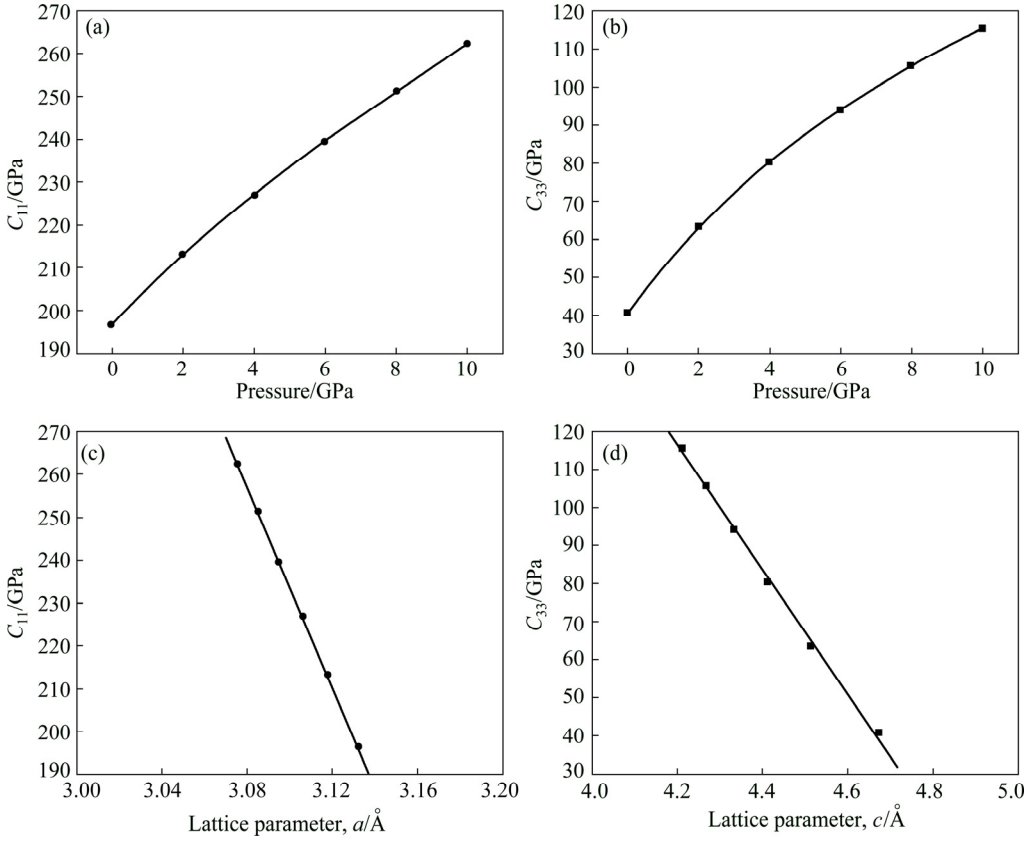

Fig. 3 Elastic constants of $Mg(OH)_2$: C_{11} (a) and C_{33} (b) vs pressure; C_{11} vs lattice parameter a (c) and C_{33} vs lattice parameter c (d)

shows that the pressure has much influence on the mechanical properties. The pressure also has great influence on the lattice parameters. The elastic constant C_{11} increases from 196.6 GPa to 262.5 GPa (ΔC_{11}= 65.9 GPa) when the pressures vary from 0 to 10 GPa. C_{33} increases from 40.8 GPa to 115.6 GPa (ΔC_{33}= 74.8 GPa). Meanwhile, lattice parameter a reduces from 3.13306 Å to 3.07708 Å (Δa=−0.05598 Å), and c reduces from 4.66946 Å to 4.21223 Å (Δc=−0.45723 Å). C_{11} and C_{33} are shown as a function of a and c in Figs. 3(c) and (d), respectively. The relationship is nearly linear and the fitting results are as Eqs. (12) and (13), and the correlation coefficients (R^2) are −0.99904 and −0.99991, respectively.

$$C_{33}=807.78691-164.5917c,\ R^2=-0.99904 \quad (12)$$

$$C_{11}=3863.17156-1170.2794a,\ R^2=-0.99991 \quad (13)$$

Table 6 lists the experimental [28,29] and calculated mechanical properties such as bulk modulus (K), shear modulus (G), shear velocity, and longitude velocity, which contain information regarding the hardness of a material with respect to various types of deformation. Two different definitions (Reuss and Voight) were given. The bulk modulus (39.6 GPa) is derived from the XRD pattern using the Birch–Murnagham equation of state by XIA et al [28] and FEI and MAO [29]. The calculations of these mechanical properties have proved the potentials' reliability as well.

Table 6 Mechanical properties of $Mg(OH)_2$

Parameter	Reuss	Voigt	Ref.
Bulk Modulus, K/GPa	36.7	69.2	This work
	36.7	55.2	Ref. [28], calculated
	39.6	−	Ref. [28], XRD
Shear Modulus, G/GPa	30.1	46.0	This work
Shear velocity/ (km·s^{-1})	30.4	39.2	Ref. [28]
	3.511	4.344	This work
Longitude velocity/ (km·s^{-1})	3.574	4.065	Ref. [28]
	5.609	7.316	This work
	5.697	6.724	Ref. [28]

3.3 First principles study of $Mg(OH)_2$ containing point defects

Firstly, structural information for $Mg(OH)_2$ containing dopant point defects in bulk, such as the crystal parameters and bond length (M—O, M=Mg, Ca, Al, Fe, and Zn, refer to Fig. 2(a)), is calculated as shown in Table 7 based on minimizing the energy.

The band structure, electron-density difference, and PDOS (partial density of states) of the doped atoms are shown in Figs. 4, 5, and 6(a), respectively. The band gap is calculated from the bottom of the valence band to the top of the conductive band. Except for Fe-doped $Mg(OH)_2$, all band gaps in the defected $Mg(OH)_2$ decreased. In the electron-density difference map, blue represents a lack of electrons, and red represents a gathering of electrons. The plane of the electron-density difference parallels to the z axis, and cuts through atoms M, O, and H.

Table 7 Crystal structure of $Mg(OH)_2$ with doped-defect in bulk

Parameter	Bulk perfect	Mg-doped defect			
		Ca	Al	Fe	Zn
a/Å	9.486	9.521	9.472	9.482	9.493
c/Å	23.793	23.805	24.101	23.755	23.479
V/Å^3	1854.550	1868.990	1872.950	1850.000	1832.35
M—O/Å	2.094	2.288	1.829	2.068	2.150
Population	0.220	0.030	0.330	0.220	0.130
Band gap/eV	3.586	3.541	3.222	3.605	3.425
Type of semi-conductor	p–type	p–type	n–type	n–type	p–type

Secondly, optimized $Mg(OH)_2$ structure containing defect was also studied by calculating the X-ray diffraction (XRD) pattern at a radiation wavelength of 1.5406 Å using Accelrys' Reflex software as shown in Fig. 7. The calculated powder XRD pattern reproduces the peak positions for all of the hexagonal $Mg(OH)_2$ structures (JCPDS file number 07−239). There were no additional phase peaks in the XRD patterns because the defect content is relatively low (1:45), and the defected element replaces Mg directly at the lattice positions. It was not easy to determine the position of a defect or experimentally insert one. Compared with pure $Mg(OH)_2$, the intensities of the (001) plane for Al- and Fe-doped $Mg(OH)_2$ increase. The diffraction intensity decreases for peak (001) in the Zn-doped Mg. The peak intensities for the Ca-doped $Mg(OH)_2$ change slightly.

Thirdly, a (001) surface containing doped point defects after geometry optimization was studied. Similar to the doped bulk defects, all of the $Mg(OH)_2$ crystal parameters for surface (001) with doped defect increase relative to a perfect crystal. The band structures are very similar as shown in Fig. 4. The band gaps are 3.198, 3.315, 3.340, 4.016 eV for Al, Zn, Ca, and Fe-doped $Mg(OH)_2$-(001), respectively. PDOS of surface (001) with defect is shown in Fig. 6(b).

4 Discussion

As for flame retardants, the most important properties are the decomposition temperature, the mechanical properties and the compatibility. It is necessary to understand the principle of flame retardants for complex $Mg(OH)_2$ and nature through modification.

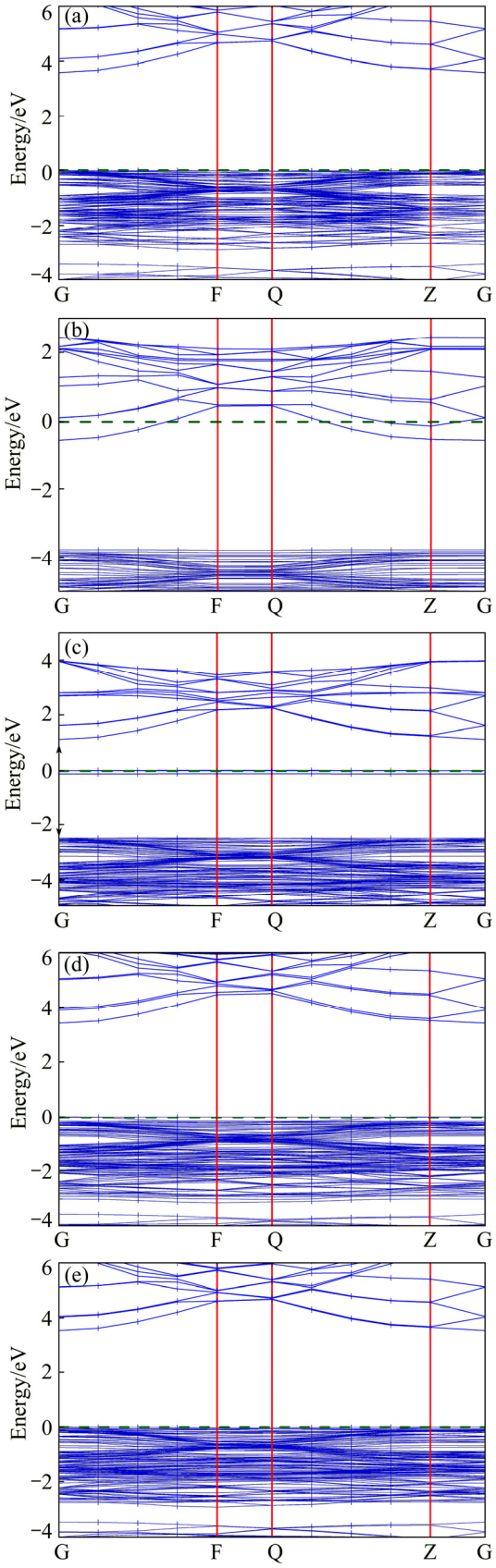

Fig. 4 Band structure at Fermi level for $Mg(OH)_2$ without defects and with defect of Al, Fe, Zn, Ca: (a) Perfect $Mg(OH)_2$; (b) Mg doped with Al; (c) Mg doped with Fe; (d) Mg doped with Zn; (e) Mg doped with Ca

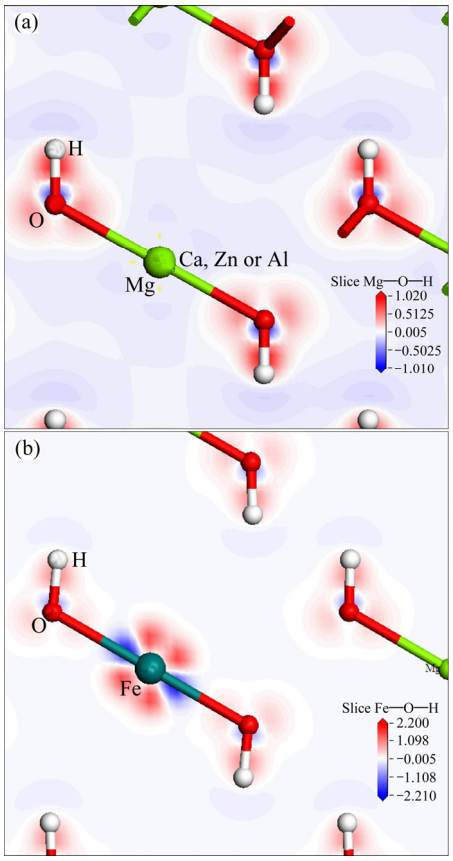

Fig. 5 Electron-density difference for $Mg(OH)_2$ containing defects of Mg, Ca, Zn, Al (a) and Fe (b)

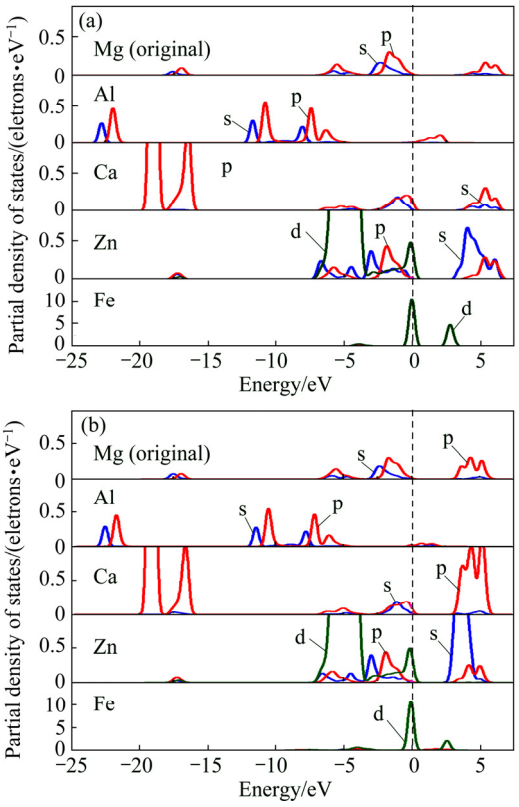

Fig. 6 PDOS of $Mg(OH)_2$ with defects in bulk (a) and on surface (001) (b)

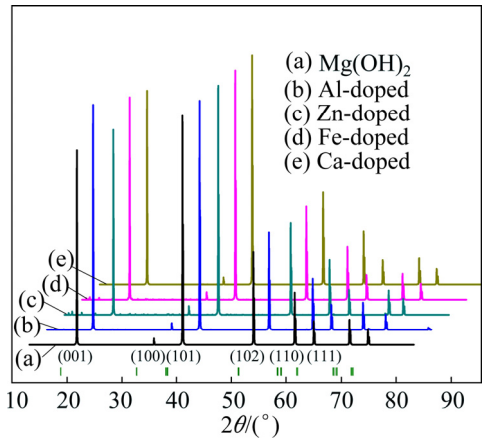

Fig. 7 Calculated XRD patterns of $Mg(OH)_2$ containing defects of Ca, Zn, Al and Fe

Defect energy calculation shows that the most unfavorable defect was the OH Schottky defect (36.342 eV) because of the strong Coulombic interaction between Mg and O. Thus, this defect rarely occurred compared with the other types of defects. The strong OH bond (OH Schottky) may sufficiently increase the internal energy barrier of dehydration to offset the entropic gain. Moreover, the enhanced H bonding (H Frenkel, 17.239 eV and H Schottky, 20.364 eV) may adequately increase the dehydration energy to a value higher than that of the gain in entropy. According to SHERMAN [30], dipole–dipole forces exist between opposing OH ions in $Mg(OH)_2$. Regarding flame retardant fillers, the decomposition temperature of a material must be sufficiently high to incorporate the filler into the polymer [31]. Based on the defect energy analysis, $Mg(OH)_2$ can sustain a high thermal decomposition temperature and facilitate modification to satisfy different uses of flame retardant fillers.

Mechanical properties should be taken into account when $Mg(OH)_2$ is to be used as additives into polymers. As for mechanical properties of $Mg(OH)_2$, the compression and expansion of c axis reflect the interactions of H—O bond and atoms between interlayer of $Mg(OH)_2$. The elastic constant C_{11} (Table 5) is about four times greater than C_{33}. This pattern is related to the layered structure in which the chemical bonding between the layers and along the layers is different [28]. Moreover, the changes of c are greater than those of a from Fig. 3. The variation rate of C_{11} with a is greater than that of C_{33} with c from the fitting Eqs. (12) and (13). The elastic constant increases because the lattice parameters decrease with pressure, which enhances the binding force between ions. Such a behavior would indicate that the O—H bond length hardly shortens by considering the effect of pressure on the layered CdI_2-type crystal structure. The result shows that the elastic properties parallel to the layers are significantly influenced by the pressure, and the ability of $Mg(OH)_2$ to anti-elastic deformation of a-axis (parallel to the layers) is superior to that of c-axis (perpendicular to the layers). Therefore, we can conclude that $Mg(OH)_2$ doped with Ca and Zn with bigger simulated crystal parameter a can undergo bigger pressure than that doped with Al and Fe from Table 7. Flame retardant fillers are used at high loadings to produce a useful effect. The filler properties such as the mechanical properties are of great importance if useful composite properties are maintained. Therefore, we should choose the materials with a special morphology such as nano-sheets [32,33] as flame retardant additives in order to avoid destroying the mechanical properties of raw material and achieve a good mechanical processing performance.

Modification through defect to get special morphology $Mg(OH)_2$ is the most widely used method. The Ca interstitial defect was found to be strongly favorable because of the negative energies, and there will be a small portion of interstitial defects depended on the synthesis conditions. The Ca substitution defect was also favorable (3.984 eV). Thus, modifying $Mg(OH)_2$ by introducing other ions is relatively easy [11], and dopant defects in bulk and surface (001) were studied in detail via first principles.

Both the Fe- and Al-doped $Mg(OH)_2$ are n-type semi-conductors from Fig. 4, which have lower system energies than p-type semi-conduct. Compared with the data shown on Figs. 6(a) and 6(b), the intensity of the valence band on surface is stronger than that in bulk. Doped defect in the surface (001) had a greater impact on the $Mg(OH)_2$ properties than that in the bulk.

$Mg(OH)_2$ with a nano-sheets morphology is suitable for combining with polymers [34]. Figure 7 shows how all of the observed intensity peaks differed in term of the reflections about the (101) plane, especially the (001) plane. The intensity of the (001) plane followed a descending order from Al- to Fe- to pure to Ca- to Zn-doped $Mg(OH)_2$. Larger values for c result in weaker H—H interactions between layers, which may create lamellar products more easily. Therefore, forming an $Mg(OH)_2$ nano-sheets with a strength of (001) is simple when there is a substitution defect of Al or Fe. The analysis of the bond population shows that the M—O bond length in an n–type $Mg(OH)_2$ crystal defected with Al and Fe was smaller than for the p–type $Mg(OH)_2$ crystal defected by Ca and Zn whether the defect existed in bulk or on surface (001). The M—O bond reflected the $Mg(OH)_2$ interactions, which were very strong when the bond is short. Therefore, this bond indicates the effects of Ca- and Zn-doped defects are small, while Al-doped defects benefit for lamellar formations. This conclusion fits with COSTA's research [35] on Mg−Zn

LDH and HDS using DFT and with the experimental results of PANG [11]. If Al- or Fe-doped defects exists, the growth of plane (001) can be enhanced by their strong covalence (populations are 0.33 and 0.22, respectively) and short bond length. Meanwhile, the growth in [001] direction can be suppressed by using a large *c* parameter. Therefore, the transitive formation of $Mg(OH)_6^{4+}$ can easily form $Mg(OH)_2$ with a large diameter-to-thickness ratio. There will be little effect when the doped element is Ca or Zn.

On the other hand, there are three transitional zones near the Fermi level for the Fe-doped $Mg(OH)_2$ that were created from orbital d of the Fe from Fig. 4, which could ease the electron transitions despite having a wider band gap than ideal for $Mg(OH)_2$ (3.605 eV > 3.586 eV). Combining the atomic charge, length and population of the bonds in Table 3 and Fig. 5(b) indicates that the effects on Fe-doped $Mg(OH)_2$ were the largest for all of the doped $Mg(OH)_2$. Meanwhile, the d orbital electrons from Zn are in a fully filled band and have little effect on the semi-conductive properties. Therefore, the electrons in the d orbital of Fe (Fig. 4(c)) changed the semi-conductive properties.

5 Conclusions

1) $Mg(OH)_2$ can provide a high level of flame retardancy because the strong OH bond and H bond sufficiently increased the internal energy barrier of dehydration to a value higher than that of the entropic gain.

2) $Mg(OH)_2$ with special morphology such as nano-sheets is the first priority considering the composite mechanical properties. Point defect energy calculation showed that Schottky defect formation was more difficult than Frenkel defect formation. $Mg(OH)_2$ facilitated modification to satisfy the different uses of flame retardant fillers because of the strong, favorable interstitial defect.

3) Elemental dopants containing un-filled electrons in their d orbitals strongly affected the doped $Mg(OH)_2$ properties. Moreover, point defects on the surfaces had even greater impact on the $Mg(OH)_2$ properties than those in the bulk.

References

[1] LI B, CAO H, YIN G. $Mg(OH)_2$@reduced graphene oxide composite for removal of dyes from water [J]. Journal of Materials Chemistry, 2011, 21(36): 13765−13768.

[2] SUIHKONEN R, NEVALAINEN K, ORELL O, HONKANEN M, TANG L, ZHANG H, ZHANG Z, VUORINEN J. Performance of epoxy filled with nano- and micro-sized magnesium hydroxide [J]. Journal of Materials Science, 2012, 47(3): 1480−1488.

[3] CAO H, ZHENG H, YIN J, LU Y, WU S, WU X, LI B. $Mg(OH)_2$ complex nanostructures with superhydrophobicity and flame retardant effects [J]. The Journal of Physical Chemistry C, 2010, 114(41): 17362−17368.

[4] SUPPAKARN N, JARUKUMJORN K. Mechanical properties and flammability of sisal/PP composites: Effect of flame retardant type and content [J]. Composites Part B: Engineering, 2009, 40(7): 613−618.

[5] AL-OWAIS A, EL-MOSSALAMY E, SHAH M, ARAFA H M. Fabrication of magnesium hydroxide nanoneedles [J]. Chemistry and Technology of Fuels and Oils, 2011, 47(2): 151−156.

[6] SAIN M, PARK S H, SUHARA F, LAW S. Flame retardant and mechanical properties of natural fibre-PP composites containing magnesium hydroxide [J]. Polymer Degradation and Stability, 2004, 83(2): 363−367.

[7] LIU S P, YING J R, ZHOU X P, XIE X L, MAI Y W. Dispersion, thermal and mechanical properties of polypropylene/magnesium hydroxide nanocomposites compatibilized by SEBS-g-MA [J]. Composites Science and Technology, 2009, 69(11−12): 1873−1879.

[8] LIU S, YING J, ZHOU X, XIE X. Core-shell magnesium hydroxide/ polystyrene hybrid nanoparticles prepared by ultrasonic wave-assisted in-situ copolymerization [J]. Materials Letters, 2009, 63(11): 911−913.

[9] FOCKE W, MOLEFE D, LABUSCHAGNE F J W, RAMJEE S. The influence of stearic acid coating on the properties of magnesium hydroxide, hydromagnesite, and hydrotalcite powders [J]. Journal of Materials Science, 2009, 44(22): 6100−6109.

[10] LI Y, SUI M, DING Y, ZHANG G, ZHUANG J, WANG C. Preparation of $Mg(OH)_2$ nanorods [J]. Advanced Materials, 2000, 12(11): 818−821.

[11] PANG H, NING G, GONG W, YE J, LIN Y. Directed tuning of nanostructure from 1D to 3D by doping diverse valent cations [J]. RSC Advances, 2011, 1(2): 184−186.

[12] PANG H, NING G, GONG W, YE J, LIN Y. Direct synthesis of hexagonal $Mg(OH)_2$ nanoplates from natural brucite without dissolution procedure [J]. Chemical Communications, 2011, 47(22): 6317−6319.

[13] TANG X, LÜ H, ZHANG Q, ZHAO J, LIN Y. Study on interactions between cadmium and defects in Cd-doped ZnO by first-principle calculations [J]. Solid State Sciences, 2011, 13(2): 384−387.

[14] DENG W, HUANG Y Y, BRUSA R S, KARWASZ G P, ZECCA A. Positron annihilation in B-doped and undoped single and polycrystalline Ni_3Al alloys [J]. Journal of Alloys and Compounds, 2006, 421(1−2): 228−231.

[15] GIORGETTI M, BERRETTONI M, SCACCIA S, PASSERINI S. Characterization of sol-gel-synthesized $LiFePO_4$ by multiple scattering XAFS [J]. Inorganic Chemistry, 2006, 45(6): 2750−2757.

[16] WANG G X, NEEDHAMA S, YAO J, WANG J Z, LIU R S, LIU H K. A study on $LiFePO_4$ and its doped derivatives as cathode materials for lithium-ion batteries [J]. Journal of Power Sources, 2006, 159(1): 282−286.

[17] SHARMA N, PETERSON V K, ELCOMBE M M, AVDEEV M, STUDER A J, BLAGOJEVIC N, YUSOFF R, KAMARULZAMAN N. Structural changes in a commercial lithium-ion battery during electrochemical cycling: An in situ neutron diffraction study [J]. Journal of Power Sources, 2010, 195(24): 8258−8266.

[18] ZHANG Mei-guang, YAN Hai-yan, WEI Qun, HUANG Duo-hui. Elastic and thermodynamic properties of Re_2N at high pressure and high temperature [J]. Transactions of Nonferrous Metals Society of China, 2013, 23(12): 3714−3721.

[19] BRAHMIA M, BENNECER B, HAMIDANI A. Electronic and optical properties of the orthorhombic compounds FeX_2 (X=P, As and Sb) [J]. Materials Science and Engineering B, 2013, 178(18): 1249−1256.

[20] ZHAO Cui-hua, CHEN Jian-hua, LI Yu-qiong, HE Qin, WU Bo-zeng. Electronic structure and flotation behavior of complex mineral jamesonite [J]. Transactions of Nonferrous Metals Society of China, 2015, 25(2): 590−596.
[21] ZENG Q H, WONG K, YU A B. Molecular dynamics simulation of Au−TiO_2 catalysts: Deposition of gold nanoclusters on rutile (110) surface [J]. Advanced Materials Research, 2011, 418−420: 870−875.
[22] GUO Yong-bo, LIANG Ying-chun. Atomistic simulation of thermal effects and defect structures during nanomachining of copper [J]. Transactions of Nonferrous Metals Society of China, 2012, 22(11): 2762−2770.
[23] MOMMA K, IZUMI F. VESTA: A three-dimensional visualization system for electronic and structural analysis [J]. Journal of Applied Crystallography, 2008, 41(3): 653−658.
[24] GALE J D, ROHL A L. The general utility lattice program (GULP) [J]. Molecular Simulation, 2003, 29 (5): 291−341.
[25] GALE J D. Empirical potential derivation for ionic materials [J]. Philosophical Magzine B, 1996, 73(1): 3−19.
[26] CATTI M, FERRARIS G, HULL S, PAVESE A. Static compression and H disorder in brucite, $Mg(OH)_2$, to 11 GPa: A powder neutron diffraction study [J]. Physics and Chemistry of Minerals, 1995, 22(3): 200−206.
[27] SEGALL M D, LINDAN P J D, PROBERT M J, PICKARD C J, HASNIP P J, CLARK S J, PAYNE M C. First-principles simulation: Ideas, illustrations and the CASTEP code [J]. Journal of Physics: Condensed Matter, 2002, 14: 2717−2744.
[28] XIA X, WEIDNER D J, ZHAO H. Equation of state of brucite: Single-crystal Brillouin spectroscopy study and polycrystalline pressure-volume-temperature measurement [J]. American Mineralogist, 1998, 83: 68−74.
[29] FEI Y, MAO H K. Static compression of $Mg(OH)_2$ to 78 GPa at high temperature and constraints on the equation of state of fluid H_2O [J]. Journal of Geophysical Research B, 1993, 98(7): 11875−11884.
[30] SHERMAN D M. Hartree-fock band structure, equation of state, and pressure induced hydrogen bonding in brucite, $Mg(OH)_2$ [J]. American Mineralogist, 1991, 76: 1769−1772.
[31] ROTHON R N, HORNSBY P R. Flame retardant effects of magnesium hydroxide [J]. Polymer Degradation and Stability, 1996, 54(2−3): 383−385.
[32] JEEVANANDAM P, MULUKUTLA R S, YANG Z, KWEN H, KLABUNDE K J. Nanocrystals to nanorods: A precursor approach for the synthesis of magnesium hydroxide nanorods from magnesium oxychloride nanorods starting from nanocrystalline magnesium oxide [J]. Chemistry of Materials, 2007, 19(22): 5395−5403.
[33] FAN W, SUN S, SONG X, ZHANG W, YU H, TAN X, CAO G. Controlled synthesis of single-crystalline $Mg(OH)_2$ nanotubes and nanorods via a solvothermal process [J]. Journal of Solid State Chemistry, 2004, 177(7): 2329−2338.
[34] ZHANG D, ZHANG P, SONG S, YUAN Q, YANG P, REN X. Simulation of magnesium hydroxide surface and interface [J]. Journal of Alloys and Compounds, 2014, 612: 315−322.
[35] COSTA D G, ROCHA A B, SOUZA W F, CHIARO S S X, LEITÃO A A. Structural and energetic analysis of $Mg_xM_{1-x}(OH)_2$ (M=Zn, Cu or Ca) brucite-like compounds by DFT calculations [J]. The Journal of Physical Chemistry C, 2008, 112(29): 10681−10687.

阻燃用含缺陷氢氧化镁的原子尺度模拟

张冬云[1,2,3]，杨 萍[1]，都 政[2]，袁秋华[1]，宋申华[3]，任祥忠[1]，张培新[1]

1. 深圳大学 化学与环境工程学院，深圳 518060；
2. 国家超级计算深圳中心，深圳 518055；
3. 哈尔滨工业大学深圳研究生院 材料科学与工程学院，深圳 518055

摘 要：采用分子动力学方法研究氢氧化镁的力学性能和点缺陷能，而对体相和表面所含点缺陷的微观电子结构采用第一性原理进行研究。结果表明，根据缺陷能分析，阳离子间隙和置换缺陷非常容易产生，因此对于氢氧化镁通过引入其他阳离子进行改性相对容易。高的 OH 键(OH Schottky 缺陷)或 H 键(H 的 Frenkel 缺陷和 Schottky 缺陷)提高了氢氧化镁脱水过程所获得熵的能垒，从而提高了氢氧化镁的分解温度，这是氢氧化镁能够满足填充型阻燃添加剂的要求本质原因之一。建立了氢氧化镁 MD 模拟的势能模型，通过模拟计算揭示了氢氧化镁晶体结构与力学性能的关系。为了获得具有较好机械加工性能的添加型阻燃剂，应选薄层状氢氧化镁。确定了含点缺陷氢氧化镁的电子结构。揭示了离子掺杂对氢氧化镁晶体的影响机制，为掺杂离子的选择提供了理论指导。

关键词：氢氧化镁；密度泛函理论；分子动力学；缺陷；电子结构

(Edited by Yun-bin HE)